Reaction Kinetics, Mechanisms and Catalysis (2023) 136:507–522
https://doi.org/10.1007/s11144-022-02337-0

Physico-chemical properties of the spinel $CaFe_2O_4$ synthesized by sol–gel route: application to drimarene green X-3G photodegradation

D. Berdous[1] · H. Kenfoud[2] · M. Trari[3]

Received: 17 October 2022 / Accepted: 16 December 2022 / Published online: 22 December 2022

Abstract

In this contribution, we report the optical and photo-electrochemical characterizations of the ferrite spinel $CaFe_2O_4$. The oxide was synthesized by sol–gel route using Polyvinylpyrrolidone organic polymer (PVP K30). The phase was confirmed by X-ray diffractometry (XRD) and a crystallite size of 51 nm was determined from the Williamson-Hall plot. The analysis by UV–Vis diffuse reflectance provided an indirect optical transition of 1.75 eV, assigned to the crystal field splitting of *3d* orbital of Fe^{3+} in six-fold coordination. The electrochemical properties were investigated in Na_2SO_4 (0.1 M) to confirm the stability of the spinel and to evaluate its photocatalytic performance. *p*-type semiconductor was shown from the capacitance measurement with a flat band potential (E_{fb}) of 0.48 $V_{Ag/AgCl}$ and holes density (N_A) of 3.66×10^{19} cm^{-3}. The Electrochemical Impedance Spectroscopy (EIS) showed a depressed semicircle at high frequencies with the existence of a double-layer capacitance (C_{dl}) followed by a Warburg diffusion (W_r). The bulk resistance in the dark (27 Ω cm^2) decreases down to 22.9 Ω cm^2 under illumination confirming the semi-conductivity. The conduction band (−1.10 V), made up of Fe^{3+}: e_g orbital, is more cathodic than the $O_2/O_2^{\cdot-}$ level (~ −0.5 V). The photo-catalysis was assessed through the oxidation of Drimarene Green X-3G (DGX) a recalcitrant and hazardous dye upon visible irradiation (16 mW cm^{-2}), through the radicals $O_2^{\cdot-}$. A conversion yield of ~ 45% is achieved at free pH, a catalyst dose of 1 g/l and DGX solution 10 mg/l within 4 h of illumination. The photodegradation obeys second-order kinetic with a photocatalytic half-life of 48.87 h.

Keywords Spinel $CaFe_2O_4$ · Electrochemical · Drimarene Green X-3G · Photodegradation · Visible light

✉ H. Kenfoud
hamza.kenfoud.93@gmail.com

Extended author information available on the last page of the article

Introduction

One of the most important concerns of our time is the energy and water supply [1, 2]. Indeed, the growing demography and accelerated industrialization, lead to the release of large quantities of all kinds of pollutants. (metals, pesticides, dyes, drugs, etc…) [3–5]. The presence of these pollutants in the aquatic environment even at concentrations represents a serious threat to the ecosystem and human health. Therefore, our planet requires quick strategies to save the environment from this pollution [6–8]. One of the main sources of pollution comes from liquid dyestuffs waste with a global production equivalent of 800,000 tons per year, including dyes discharged from the food, detergent and textile industries [9, 10]. They are classified as hazardous compounds with harmful effects on living organisms and inhibit considerably the photosynthesis by reducing the penetration of light into the water [11, 12]. To meet these challenges and avoid any harm to the environment, it is necessary to proceed to their elimination before they are discharged into waterways. Among the alternatives for removing these harmful organics, one can cite biosorption [13], chemical oxidation [14], burning [15], biodegradation and membrane separation [16]. However, these methods remain rather limited because they are expensive and often difficult to implement; in addition, incomplete oxidation needs additional organic processing [17]. To overcome these drawbacks, advanced oxidation processes (AOPs) are used as a "green" strategy in water research to get rid of organic matter and prevent pollution [18]. In this respect, the solar photocatalysis has emerged as a clean alternative for its efficacy under soft conditions [19, 20]. Semiconductors such as TiO_2, SnO_2 and $BaTiO_3$ are photo-electrochemically stable and have been used in environmental photocatalytic applications [21–23]. However, their photo-responses are restricted to UV light due to the wide optical gap (E_g) and are therefore of little practical use with respect to solar emissions which account for only about 5% of sunlight [24, 25]. In this regard, continued interest in photocatalysis has led to significant experimental work on narrow band gap semiconductors like delafossites [26], perovskites [27] and spinels [28] which gave satisfactory results in the H_2 production and oxidation of organics [29–31]. In the spinels, the electrons are excited in a conduction band (CB) made up of *3d* orbitals with energy high enough to reduce dissolved oxygen to $O_2{\cdot}-$ radicals and water to gaseous hydrogen. [32]. Importantly, the energy of the valence band (VB), consisting also of *3d* character, is raised, thus shifting the spectral photoresponse to the visible light region. The spinels are among our most researched photocatalysts due to their low cost, friendly environmental characteristics, narrow band gap and magnetic properties [33, 34].

Therefore, our research program was partially directed toward the spinel family AB_2O_4 [35]. Based on the above contents, we report in this contribution the characterizations of $CaFe_2O_4$ synthesized by chemical route. It has remarkable magnetic and catalytic properties due to its ability to absorb half of the solar spectrum and convert it into chemical and/or electrical energy ($E_g \sim 2$ eV) [36].

Optimization by such operational factors as catalyst dose, dye concentration and photocatalyst recycling potential. This research aimed to study the photoelectrochemical properties and photocatalytic activity of $BaFe_2O_4$ nanoparticles and

to explore the possibility of using them in the photocatalysis of DGX under visible light irradiation.

Many dyes are weakly biodegradable and therefore not easy to oxidize by classical techniques. The morphology of the catalyst (porosity, roughness and specific surface area) has a considerable influence on the photocatalytic performance, and decreasing the crystallite size improves the dye photo-oxidation because of enhanced surface areas. The spinel is a low polaron hopping semiconductor, and the lifetime of the electron/hole (e^-/h^+) pairs must be long enough to reach the liquid interface and to contribute to photo-electrochemical reactions. For this, we have chosen the hydrothermal route for preparing fine powders with an enhanced surface-to-volume ratio.

Experimental

Synthesis of material

$CaFe_2O_4$ was prepared by sol–gel route using polyvinylpyrrolidone K30 (PVP K30) as a combustion agent. $Ca(NO_3)_2$, $6H_2O$ (Fluka, 98%) and $Fe(NO_3)_3$, $9H_2O$ (Biochem, 98%) previously stored in a desiccator under static vacuum, were dissolved separately in ethanol under stirring; an excess of 5% citric acid was added to the solutions. Then the solutions were mixed in 200 ml of water and heated at 60 °C for 2 h. PVP K30 dissolved in water was added dropwise to the mixing solution. After evaporation at 100 °C (20 h), the mixture turned into a black gel, which was burned at 300 °C and the auto combustion gave a xerogel. The latter was ground in an agate mortar and heat-treated in the air at 850 °C (8 h, 5 °C/min) in an alumina crucible to remove the carbonaceous residue that remained after the combustion. The fine brown powder was stored in an airtight bottle until use. Distilled water was used in all preparations.

Characterization methods

The X-ray diffraction (XRD) was carried out with a PANalytical X-ray diffractometer (Cu K_α line, $\lambda = 1.54056$ Å) at a scanning rate of 0.01°/s in the range (10–90°).

The diffuse reflectance of the spinel was plotted with a Jasco 650 Ultraviolet–Visible spectrophotometer which goes from 190 to 900 nm using $BaSO_4$ as a reference. The powder was pressed into dense pellets ($\varnothing = 13$ mm, thickness ~ 0.8 mm) under 300 MPa and fired at 900 °C, yielding a compactness of 92% with good mechanical properties.

The electrochemical study was realized in a Pyrex cell, which permitted the introduction of the reference electrode, Pt counter electrode and the working electrode (WE). The potentials were given against Ag/AgCl, which refers to a saturated potassium chloride (KCl) electrolyte. The electrodes are immersed in Na_2SO_4 (0.1 M) solution and piloted by a PGZ 301 Potentiostat at a rate of 10 mV s^{-1}. The capacity characteristic (C) was studied at 10 kHz and the electrochemical impedance

spectroscopy (EIS) was measured in the range (10^{-2}–10^{5} Hz), once the open circuit potential (OCP) was stabilized.

Photocatalytic study

The photocatalytic oxidation of DGX was carried out in a double-walled Pyrex reactor connected to a thermo-stated bath (25 °C). The $CaFe_2O_4$ powder with a mass of 300 mg was suspended in 300 ml of DGX solution (10 mg/l, free pH) by magnetic stirring; the adsorption experiment was realized in the dark for 90 min to reach the adsorption equilibrium. Then, a tungsten-halogen lamp (200 W, 16 mW/cm2) irradiated the reactor; 5 ml aliquots were periodically taken and the photocatalyst particles were separated by centrifugation (4500 rpm for 15 min). The remaining DGX concentrations were analyzed by measuring the absorbance with a UV–Vis spectrophotometer (Shimadzu 1800, $\lambda_{max} = 660$ nm). The degradation efficiency was calculated from the relationship:

$$\text{Degradation efficiency } \% = \frac{\text{abs}_{ads} - \text{abs}}{\text{abs}_{ads}} \times 100 \quad (1)$$

Here abs_{ads} and abs are the equilibrium concentrations in the dark and the absorbance after time t of DGX, respectively.

Results and discussion

Photocatalyst characterization

XRD analysis

After the synthesis and calcination steps, the phase purity and crystal structure of $CaFe_2O_4$ were confirmed by XRD analysis. The diffractogram is shown in Fig. 1. The oxide crystallizes in an orthorhombic symmetry with the lattice parameters: $a = 9.2379$ Å, $b = 10.6997$ Å and $c = 3.0202$, in agreement with the Pnma space group (N° 62) according to ICDD card No. 01-072-1199. The corrected peaks are characteristic of high purity and agree well with those previously reported [37, 38]. Except for $CaFe_2O_4$, no other diffraction peaks associated with the hematite Fe_2O_3 [39, 40], CaO or other impurities appear in the diffractogram. The structure of the spinel $CaFe_2O_4$, shown in Fig. 1 (Inset), was built thanks to the Vista software. The average crystallite size (D) was obtained from the width of the peak (β) by using the Williamson-Hall (W–H) relationship:

$$\beta \cos\theta = K\lambda / D + 4n \sin\theta \quad (2)$$

K is the form factor and π the lattice strain of $CaFe_2O_4$ powder. The β cosθ line variance as a function of 4sinθ is shown in Fig. 2. The slope and y-intercept respectively yield a lattice strain (π) of 5×10^{-5} and a crystal size (D) of 51 nm. Assuming compact and spherical crystallites, a specific surface area of ~ 28 $m^2\ g^{-1}$ is calculated

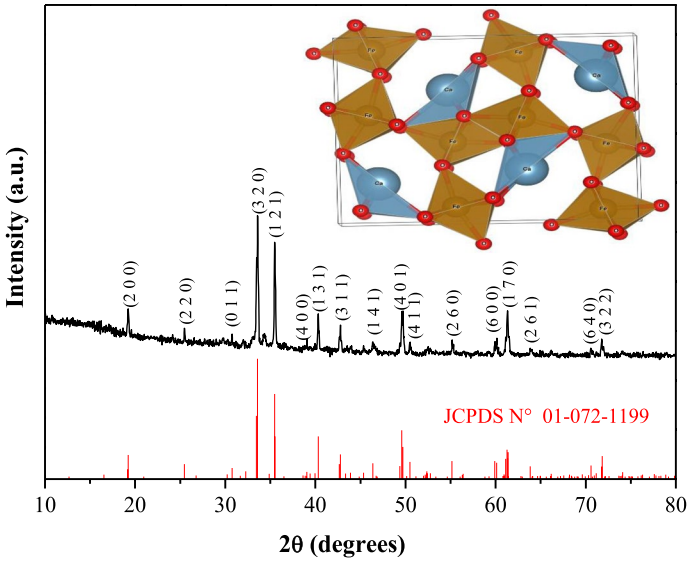

Fig. 1 X-ray diffraction pattern of $CaFe_2O_4$ prepared by sol–gel route. Inset: The structural representation of the spinel

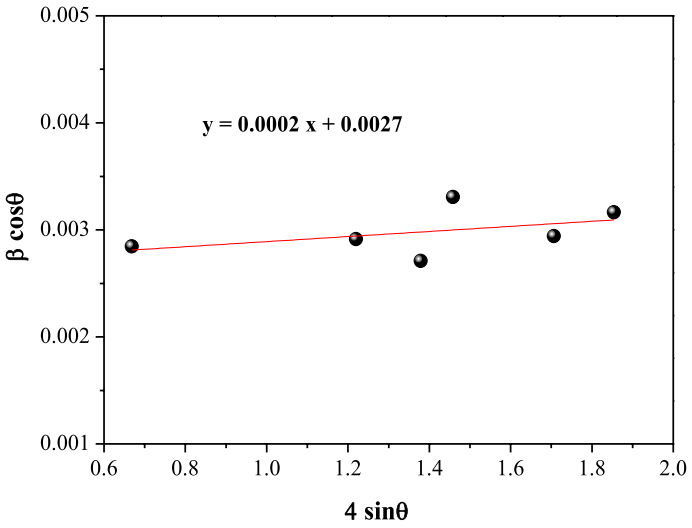

Fig. 2 The Williamson-Hall plot of $CaFe_2O_4$ prepared by sol–gel route. Nano crystals for the determination of the crystallite size

from the relation ($=6/\rho_{exp}$ D) where ρ_{exp} is the experimental density (4.19 g cm^{-3}), measured by picnometry; this value is relatively higher than that determined in previous works [41, 42], and indicates a certain porosity of the powder. It is known that

a large specific surface could provide a large number of active sites in a photocatalytic process [43].

UV–Vis analysis

The photo activity of the semiconductor is closely related to its light absorption. The optical behavior of the spinel was determined by UV visible spectrophotometry in the range of 190–900 nm. $CaFe_2O_4$ has an absorption edge (λ_o) equal to 599 nm corresponding to a gap ($\lambda_o = 1240/E_g$) with a marked absorption enhancement in the visible-light region, the gap energy (E_g) is determined from the relation:

$$(\alpha hn)^{1/k} = \text{Constant} \times \left(hn - E_g\right) \tag{3}$$

α is the absorption coefficient and its reciprocal value corresponds to the penetration depth of the monochromatic light. For the direct and indirect transition of a semiconductor, k is equal to 0.5 and 2. The intersection of the straight lines $(\alpha h\nu)^2$ and $(\alpha h\nu)^{1/2}$ with the energy-axis (Fig. 3) give direct (2.07 eV) and indirect (1.75 eV) transitions, the latter conforms with the brick red color of the powder.

Electrochemical properties

The current potential J(E) profiles plotted in Na_2SO_4 electrolyte (Fig. 4) show that the $CaFe_2O_4$ has good electrochemical stability over the entire potential range indicated by the low dark current J_d ($< \sim 1$ mA/cm^2). The peak at ~ -0.3 V is due to the reduction of dissolved oxygen ($2H_2O + O_2 + 2e^- \rightarrow H_2O_2 + 2OH^-$); it

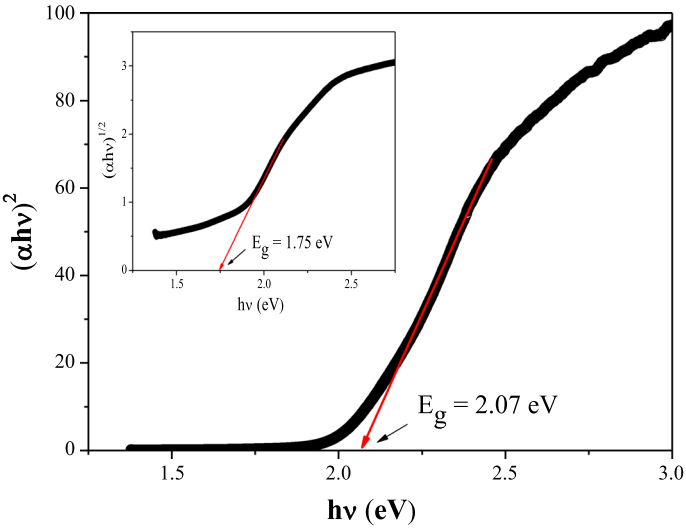

Fig. 3 The direct optical transition $(\alpha h\nu)^2$ vs. hν of $CaFe_2O_4$ prepared by sol–gel route. Inset: indirect allowed transition

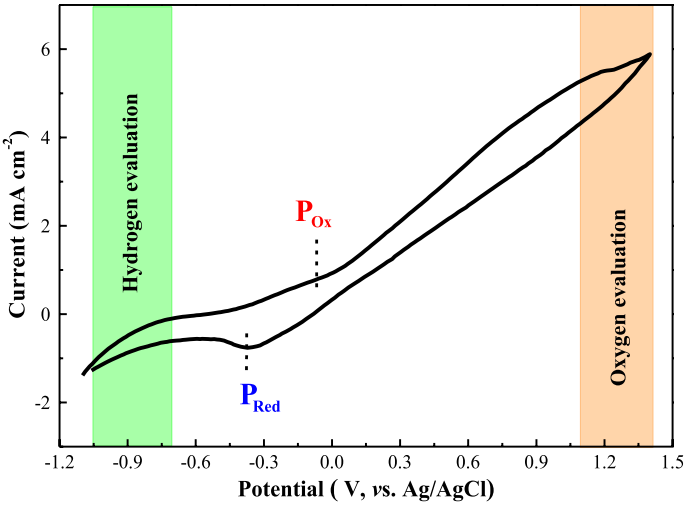

Fig. 4 Cyclic voltammetry of the electrode $CaFe_2O_4$ sintered at 850 °C in air saturated Na_2SO_4 (0.1 M) plotted at room temperature. Scan rate 5 mV/s

has been observed that the height of the peak decreases under N_2 bubbling [44]. The current increase linearly at lower potentials, due to the charge of the double layer at the electrode/solution interface. Then, the current saturation returns to a diffusion-limited process. The increased current above ~ 0.6 V is assigned to the formation of O_2 with a low over-voltage while the decrease below −0.9 V is due to the evolution of H_2 as indicated by the bubbles observed on the electrode surface.

The photocurrent onset potential (E_{on}) below which the photocurrent appears is determined according to the Gartner model [45]:

$$J_{ph}^2 = \text{Const} \times \alpha^2 W^2 \left(E - E_{on}\right) \tag{4}$$

Here α (cm^{-1}) is the absorption coefficient and W the space charge region; the potential E_{on} (−0.15 V) is deduced from the cross point of the line $J_{ph}{}^2$ (E) to E-axis (Fig. 5). In a first approximation. The interfacial capacity (C) is measured to obtain the flat band potential (E_{fb}) which is crucial to accurately determine the "potential/energy" of the electronic band and to build the band diagram in order to evaluate the photoactivity of spinel:

$$C^{-2} = \frac{2}{\varepsilon\varepsilon_0 A^2 e N_A}\left(E - E_{fb}\right) \tag{5}$$

The extrapolation of the line (C^{-2}) plot to infinite capacity (Fig. 6) gives the potential E_{fb} (0.48 V), while the negative slope implies *p*-type conduction of $CaFe_2O_4$ with holes as dominant carriers. The flattening region below ~ 0.5 V is attributed to the accumulation zone of (h^+/e^-) pairs, where their recombination

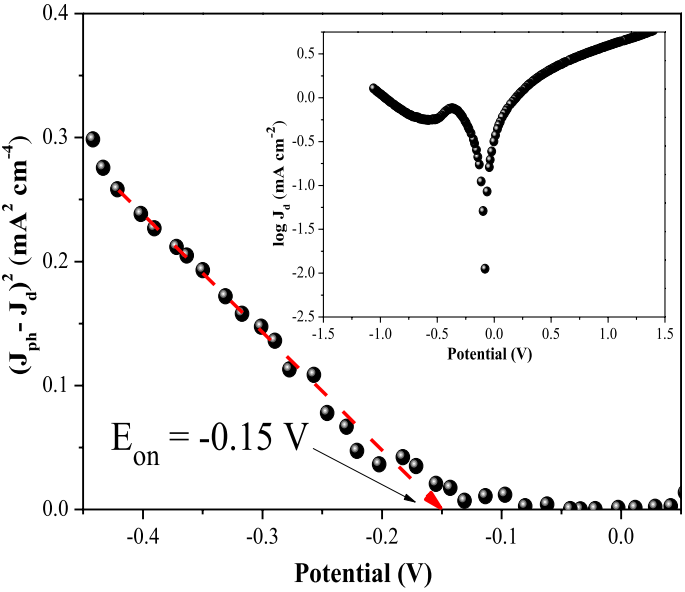

Fig. 5 The plot $(J_{ph}–J_d)^2$ vs. potential of $CaFe_2O_4$ in Na_2SO_4 (0.1 M) for the determination of the photocurrent onset potential (E_{on}) according to the Gartner model. Inset: Semi logarithmic plot electrolyte

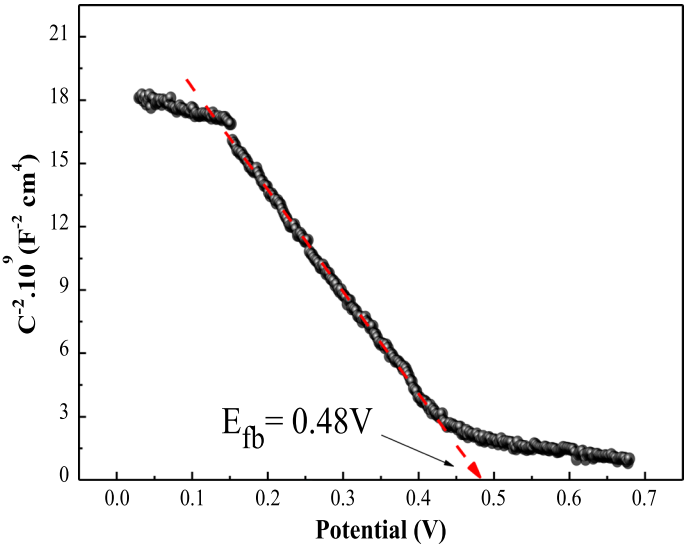

Fig. 6 The capacitance^{-2}-potential characteristic of $CaFe_2O_4$ in Na_2SO_4 (0.1 M) solution plotted at 10 kHz for the determination pf the flat band potential (E_{fb})

predominates. The discrepancy between the potentials E_{on} and E_{fb} indicates the presence of surface states within the gap region [46].

The holes density N_A (3.66×10^{19} cm^{-3}) was computed from the slope value ($m=4.82\times10^{10}$ (F^{-2} cm^4/V)) where the dielectric measurement of ($\varepsilon\sim80$) at 293 K was taken from our previous work [47]. such value extends the depletion width, an advantageous property in photocatalysis:

$$W = \left(2\,\varepsilon\varepsilon_o\,\Delta U/eN_A\right)^{1/2} \tag{6}$$

ΔU is the interfacial band bending ($E_{fb}-E$), equal to ~ 0.5 V. The term ($\Delta U\ \varepsilon\varepsilon_o/e$) is constant and the length (W ~ 11 nm) is controlled by the doping density N_A. Good photoactivity is expected when the condition ($\alpha_\lambda^{-1} < W$) is fulfilled; this condition requires a semiconductor moderately doped (N_A small) with a Fermi level of ~ 0.5 above the valence band. α_λ is the extinction coefficient of the spinel for the monochromatic light (λ).

The chemical stability is confirmed by the potentiodynamic potential plot measured in the Na_2SO_4 (0.1 M) solution, which is a common technique for checking the corrosion process. The slope $dlogJ_d/dE$ (Fig. 6 inset) gives a corrosion potential (E_{cor}) of −0.07 V and a small exchange density (J_{ex}) of 0.01 mA cm^{-2}, and therefore the oxide shows excellent chemical inertness.

The EIS graph, i.e., imaginary (Z_{im}) versus real (Z_{real}) part of the complex impedance brings insights into the reactions occurring at the solid/liquid interface and the data were recorded at the open circuit potential after its stabilization in the region ($10^{-2}-10^5$ Hz). The EIS representation exhibits two semicircles in the dark and under visible light (Fig. 7), assigned to the charge transfer resistance (R_{ct1}) and grains boundaries. A Warburg diffusion (W_r) is evidenced by the straight line inclined at 45° at low

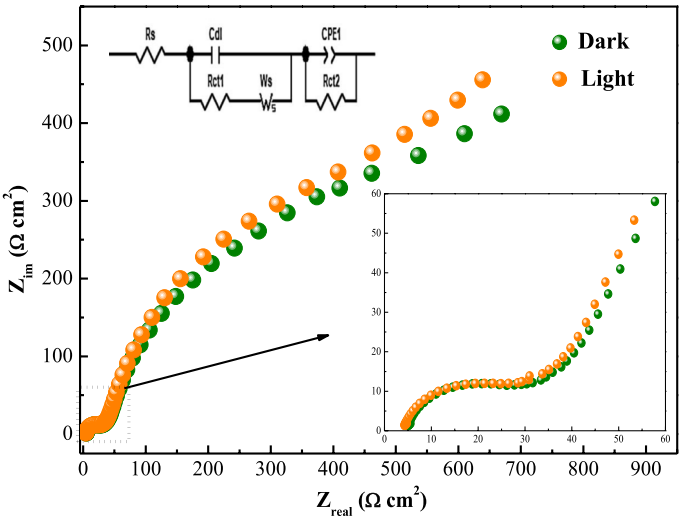

Fig. 7 Comparison of EIS diagrams of $CaFe_2O_4$ plotted at the open circuit potential in the dark and under visible light

frequencies. and these two elements are in parallel with the double layer capacity (C_{dl}) in the electrode/electrolyte interface. The R_{ct1} can be derived from the high-frequency intercept (27.1 Ω cm^2) which decreases down to 22.9 Ω cm^2 under illumination, thus corroborating the semiconducting character of the spinel. Then for the second semi-circle associated with the charge transfer resistance (R_{ct2}), the center is localized below the real axis and this comes with the existence of a constant phase element (CPE) which represents a deviation from a pure capacitive behavior. The offset from the origin (R_S) is equal to the electrolytic resistance of the Na_2SO_4 solution (0.1 M), attributed to the ionic molar conductivities at an infinite solution (Λ^{∞}) of SO_4^{2-} (~160 Ω^{-1} cm^2 mol^{-1}) and Na^+ (~50 Ω^{-1} cm^2 mol^{-1}) [48]. The EIS data are fitted to an equivalent electrical circuit (Fig. 7, Inset) and the electrochemical parameters are summarized in Table 1. The Bode representation is given in SM 1.

DGX photodegradation

To assess the photocatalytic activity of $CaFe_2O_4$, DGX was used as a model pollutant under visible irradiation. Firstly, the reaction was performed in the absence of a catalyst to explore the role of photolysis. The result showed that the seft-degradation of DGX is insignificant and is relatively stable. Before the irradiation of light, the mixture of DGX solution/photocatalyst was kept in the dark under stirring for 90 min to reach the adsorption–desorption equilibrium. Then, it was deduced from the degradation experiments that the light/catalyst system plays a crucial essential role in the photodegradation of the dye. Fig. 8 shows the evolution of the DGX concentration (10 mg/l) as a function of time under visible light illumination for a catalyst dose of 1 g/l. The maximum absorption peak at 553 nm, and 45% of the dye was photocatalytically removed within 4 h at 25 °C at free pH.

The kinetics of the DGX photodegradation onto $CaFe_2O_4$ was also considered.

Kinetics are usually represented according to pseudo-first- and second-order models respectively [49]:

$$v = \frac{-dc}{dt} = k_1 C \tag{7}$$

$$v = \frac{-dc}{dt} = k_2 C^2 \tag{8}$$

Here v is the photocatalytic rate of the degradation (mg/l min), k_1 is the first-order apparent constant of the degradation (min^{-1}), k_2 is the second order apparent

Table 1 Electrochemical parameters of $CaFe_2O_4$ in the dark and under visible light obtained by fitting the EIS data with an equivalent circuit model

	Rs (Ω)	C_{dl} (mF)	Rct_1 (Ω)	Ws ($S.sec^{1/2}$)	CPE ($S\ sec^{1/n}$)	*n*	Rct_2 (Ω)
Dark	5.56	1.93	27.1	0.004226	0.0153	0.6113	388
Light	4.78	2.47	22.9	0.004319	0.0189	0.5976	327

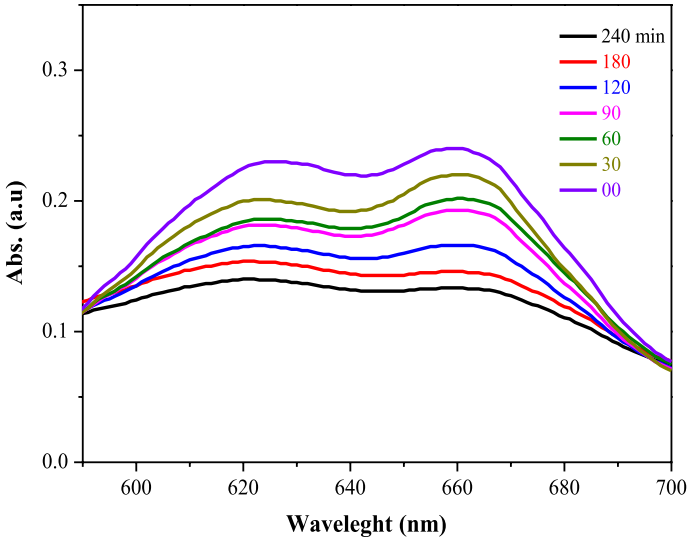

Fig. 8 The UV–Vis spectra of photo degradation of DGX (10 mg/l) on $CaFe_2O_4$ at neutral pH, 25 °C under visible light

constant of the degradation (l/mg min), C is the concentration (mg/l) and t the irradiation time (min). The integration of equations. (7 and 8) together with the determination (C=Co when t = 0) gives the following equations

$$C = C_o e^{-k\,t} \tag{9}$$

$$v = \frac{C_o}{1 + ktC_o} \tag{10}$$

Based on Fig. 9 and Table 2, we can conclude that the kinetic of photocatalysis on $CaFe_2O_4$ is well described by the second order, as indicated by the straight lines with higher correlation coefficients ($R^2 = 0.985$). The former can describe the disappearance of the DGX with an apparent kinetic constant k_{app}. This value allows us to extract the initial rate, and the photocatalytic half-life time ($t_{1/2}$) of 48.87 h is calculated using the following relationship:

$$t_{1/2} = \frac{1}{kC_o} \tag{11}$$

Photocatalytic mechanism

In order to improve the photocatalytic performance, it was interesting to develop the catalyst powder by sol–gel method with the goal reduction to length the electrons

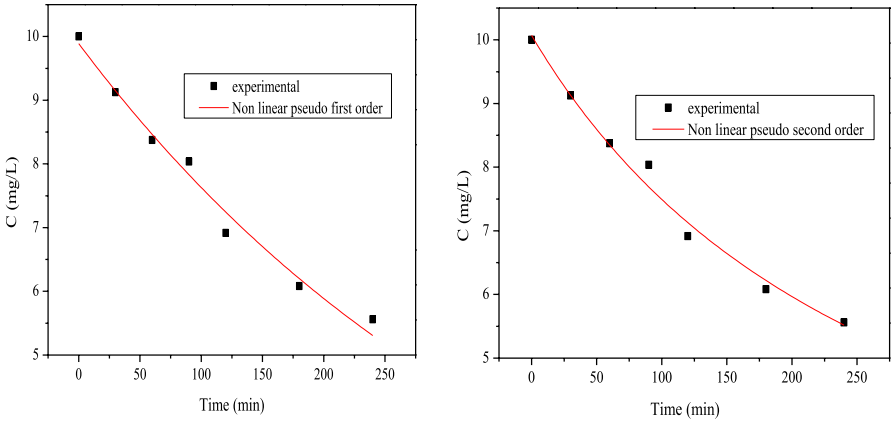

Fig. 9 The non-linear first and second order kinetics of the DGX photodegradation

Table 2 Parameters of non-linear first and second order for DGX photodegradation onto synthesized $CaFe_2O_4$

First order			Second order		
R^2	k_1 (min^{-1})	Standard error	R^2	k_2 (L/mg min)	Standard error
0.981	2.59×10^{-3}	1.55×10^{-4}	0.985	3.41×10^{-4}	1.90×10^{-5}

have to cross to reach the interface. For better elucidating the photocatalytic degradation of DGX on $CaFe_2O_4$ nanocomposites under visible irradiation, a plausible mechanism has been suggested on the basis of by energy diagram. Based on the electrical ($E_a = 0.17$ eV) optical ($E_g = 2.07$ eV) and photo-electrochemical ($E_{fb} = 0.48$ V) characterizations, where E_a is the activation energy [34], the band edge positions of the synthesized spinel are expressed as by the relations:

$$E_{VB} = eE_{fb} + E_a + 4.75 - E_g \tag{12}$$

$$E_{CB} = E_{VB} - E_g \tag{13}$$

These relationships allow us to infer potential values of the valence band (0.65 V) and conduction band (−1.10 V), where e is the elementary charge. These values indicate that both bands derive mainly from Fe^{3+}: *3d* orbital in six-fold coordination ($t_{2g}^3 \rightarrow e_g^2$) [47]. Once irradiation of the semiconductor $CaFe_2O_4$ by energetic photons ($h\nu > E_g$), the (e^-/h^+) pairs generated within the diffusion length of the semiconductor are separated by the interfacial electric field (Eq. 10). CB-$CaFe_2O_4$ (−1.10 V) is located above the level $O_2/O_2{\cdot}-$ (−0.5 V), clarifying that the electron can contribute in the DGX photo-oxidation.

Thus, the electrons react with dissolved oxygen to produce reactive $O_2{\cdot}-$. On the other hand, it is unlikely that the hole in the valence band oxidizes H_2O to

generate $^{\cdot}OH$ because the potential of VB−$CaFe_2O_4$ (0.65 V) is anodic of the couple $H_2O/^{\cdot}OH$ (2 V). Based on the above-mentioned contents, the photocatalytic degradation of DGX is suggested as follows:

$$CaFe_2O_4 + hv \rightarrow e^-_{CB} + h^+_{VB} \tag{14}$$

$$e^-_{CB} + O_2 \rightarrow O_{2^-} \tag{15}$$

$$O_2 + 2H_2O + 2e^- \rightarrow H_2O_2 + 2OH^- \tag{16}$$

$$DGX + O_{2^-} \rightarrow \text{Degradation products} \tag{17}$$

$CaFe_2O_4$ with its environmentally friendly characteristics has been tested for hydrogen production under visible irradiation. The results are promising and will be communicated very soon.

Conclusions

Conclusively, this work was dedicated to the synthesis of the spinel $CaFe_2O_4$ by a facile sol–gel process using a Polyvinylpyrrolidone organic polymer (PVP K30), followed by an exhaustive characterization through optical and electrochemical studies. These properties have confirmed the stability and *p*-type semi-conductivity of spinel, which can exploit a large part of solar radiation into chemical energy. The photo-electrochemistry enabled us to construct the energy diagram with the accurate positions of the conduction and the valence bands, a precursor to photocatalysis. Drimarene Green is a dangerous and persistent dye, released into the natural aquatic environment by uncontrolled industrial effluents. It was successfully oxidized under visible irradiation in the presence of $CaFe_2O_4$. Experimental results revealed that 45% DGX degradation by $O_2{\cdot}-$ radicals under ideal conditions, for less than 4 h of exposure under visible light irradiation. The photocatalytic oxidation followed the pseudo second-order kinetic with a photocatalytic half-life of 48.87 h.

Author contributions DB: writing—original draft preparation and investigation, HK: writing—review and editing, MT: Writing and supervising.

Funding The authors have not disclosed any funding.

Data availability Not applicable.

Declarations

Conflict of interest The authors declare no competing interests.

Ethical approval We would like to declare on behalf of my co-authors that the work described was original research that has not been published previously, and not under consideration for publication elsewhere, in whole or in part.

References

1. Asif M, Muneer T (2007) Energy supply, its demand and security issues for developed and emerging economies. Renew Sustain Energy Rev 11:1388–1413. https://doi.org/10.1016/j.rser.2005.12.004
2. Wang M, Webber M, Finlayson B, Barnett J (2008) Rural industries and water pollution in China. J Environ Manage 86:648–659. https://doi.org/10.1016/j.jenvman.2006.12.019
3. Lezier V, Gusarova M, Kopytova A (2017) Water supply of the population as a problem of energy efficiency on the example of the Tyumen region of Russia. IOP Conf Ser: Earth Environ Sci. https://doi.org/10.1088/1755-1315/90/1/012069
4. Baaloudj O, Assadi I, Nasrallah N et al (2021) Simultaneous removal of antibiotics and inactivation of antibiotic-resistant bacteria by photocatalysis: a review. J Water Process Eng 42:102089. https://doi.org/10.1016/j.jwpe.2021.102089
5. Baaloudj O, Nasrallah N, Bouallouche R et al (2022) High efficient Cefixime removal from water by the sillenite Bi12TiO20: photocatalytic mechanism and degradation pathway. J Clean Prod 330:129934. https://doi.org/10.1016/j.jclepro.2021.129934
6. Ayangbenro AS, Babalola OO (2017) A new strategy for heavy metal polluted environments: a review of microbial biosorbents. Int J Environ Res Public Health. https://doi.org/10.3390/ijerph14010094
7. Chawla L, Cushing DF (2007) Education for strategic environmental behavior. Environ Educ Res 13:437–452. https://doi.org/10.1080/13504620701581539
8. Sharma S, Sharma V, Chatterjee S (2021) Microplastics in the mediterranean sea: sources, pollution intensity, sea health, and regulatory policies. Front Mar Sci. https://doi.org/10.3389/fmars.2021.634934
9. Kishor R, Purchase D, Saratale GD et al (2021) Ecotoxicological and health concerns of persistent coloring pollutants of textile industry wastewater and treatment approaches for environmental safety. J Environ Chem Eng. https://doi.org/10.1016/j.jece.2020.105012
10. Chen HL, Burns LD (2006) Environmental analysis of textile products. Cloth Text Res J 24:248–261. https://doi.org/10.1177/0887302X06293065
11. Raj S (2008) Bio-decolourization of textile effluent containing Reactive Black-B by effluent-adapted and non-adapted bacteria. Afr J Biotechnol 7:3309–3313
12. Jothi D (2015) Application of enzyme extracted from aloe vera plant in chemical pretreatment of cotton knitted textile to reduce pollution load. World J Eng Technol 03:37–44. https://doi.org/10.4236/wjet.2015.33b007
13. Park D, Yun YS, Park JM (2010) The past, present, and future trends of biosorption. Biotechnol Bioprocess Eng 15:86–102. https://doi.org/10.1007/s12257-009-0199-4
14. Mantzavinos D, Psillakis E (2004) Enhancement of biodegradability of industrial wastewaters by chemical oxidation pre-treatment. J Chem Technol Biotechnol 79:431–454. https://doi.org/10.1002/jctb.1020
15. Gadde B, Bonnet S, Menke C, Garivait S (2009) Air pollutant emissions from rice straw open field burning in India, Thailand and the Philippines. Environ Pollut 157:1554–1558. https://doi.org/10.1016/j.envpol.2009.01.004
16. López C, Mielgo I, Moreira MT et al (2002) Enzymatic membrane reactors for biodegradation of recalcitrant compounds: application to dye decolourisation. J Biotechnol 99:249–257. https://doi.org/10.1016/S0168-1656(02)00217-1
17. Zhang D, Ghysels S, Ronsse F (2020) Effluent recirculation enables near-complete oxidation of organics during supercritical water oxidation at mild conditions: a proof of principle. Chemosphere 250:126213. https://doi.org/10.1016/j.chemosphere.2020.126213
18. Astas S (2008) Use of selected advanced oxidation processes (AOPs) for wastewater treatment—a mini review. Global NEST J 10:376–385
19. Spasiano D, Marotta R, Malato S et al (2015) Solar photocatalysis: materials, reactors, some commercial, and pre-industrialized applications: a comprehensive approach. Appl Catal B 170–171:90–123. https://doi.org/10.1016/j.apcatb.2014.12.050
20. Malato S, Fernández-Ibáñez P, Maldonado MI et al (2009) Decontamination and disinfection of water by solar photocatalysis: Recent overview and trends. Catal Today 147:1–59. https://doi.org/10.1016/j.cattod.2009.06.018
21. Suria S, Pewarna T, Jadi S, Nanohablur B (2012) 11 Khalil. 41:1011–1016

22. Liu D, Fessenden RW, Hug GL, Kamat PV (1997) Dye capped semiconductor nanoclusters: role of back electron transfer in the photosensitization of SnO2 nanocrystallites with cresyl violet aggregates. J Phys Chem B 101:2583–2590. https://doi.org/10.1021/jp962695p
23. Pare B, Jonnalagadda SB, Tomar H et al (2008) ZnO assisted photocatalytic degradation of acridine orange in aqueous solution using visible irradiation. Desalination 232:80–90. https://doi.org/10.1016/j.desal.2008.01.007
24. Zyoud AH, Zubi A, Hejjawi S et al (2020) Removal of acetaminophen from water by simulated solar light photodegradation with ZnO and TiO2 nanoparticles: catalytic efficiency assessment for future prospects. J Environ Chem Eng 8:104038. https://doi.org/10.1016/j.jece.2020.104038
25. Abo R, Kummer NA, Merkel BJ (2016) Optimized photodegradation of Bisphenol A in water using ZnO, TiO2 and SnO2 photocatalysts under UV radiation as a decontamination procedure. Drink Water Eng Sci 9:27–35. https://doi.org/10.5194/dwes-9-27-2016
26. Yin L, Shi Y, Lu L et al (2016) A novel delafossite structured visible-light sensitive AgFeO2 photocatalyst: preparation, photocatalytic properties, and reaction mechanism. Catalysts. https://doi.org/10.3390/catal6050069
27. Kanhere P, Chen Z (2014) A review on visible light active perovskite-based photocatalysts. Molecules 19:19995–20022. https://doi.org/10.3390/molecules191219995
28. Chandrasekaran S, Bowen C, Zhang P et al (2018) Spinel photocatalysts for environmental remediation, hydrogen generation, CO2 reduction and photoelectrochemical water splitting. J Mater Chem A 6:11078–11104. https://doi.org/10.1039/c8ta03669a
29. Brahimi R, Bessekhouad Y, Bouguelia A, Trari M (2007) CuAlO2/TiO2 heterojunction applied to visible light H2 production. J Photochem Photobiol, A 186:242–247. https://doi.org/10.1016/j.jphotochem.2006.08.013
30. Bessekhouad Y, Trari M (2002) Photocatalytic hydrogen production from suspension of spinel powders AMn2O4(A=Cu and Zn). Int J Hydrogen Energy 27:357–362. https://doi.org/10.1016/S0360-3199(01)00159-8
31. Saadi S, Bouguelia A, Trari M (2006) Photoassisted hydrogen evolution over spinel CuM2O4 (M=Al, Cr, Mn, Fe and Co). Renew Energy 31:2245–2256. https://doi.org/10.1016/j.renene.2005.10.014
32. Edwards PP, Egdell RG, Fragala I et al (1984) A study of the spinel materials LiTi2O4 and Li4 3Ti5 3O4 by photoelectron spectroscopy. J Solid State Chem 54:127–135. https://doi.org/10.1016/0022-4596(84)90140-3
33. Cherifi K, Rekhila G, Omeiri S et al (2019) Physical and photoelectrochemical properties of the spinel ZnCr2O4 prepared by sol gel: application to Orange II degradation under solar light. J Photochem Photobiol, A 368:290–295. https://doi.org/10.1016/j.jphotochem.2018.10.003
34. Kenfoud H, Nasrallah N, Meziani D, Trari M (2021) Photoelectrochemical study of the spinel CaFe2O4 nanostructure: application to Basic Blue 41 oxidation under solar light. J Solid State Electrochem. https://doi.org/10.1007/s10008-021-04952-8
35. Lee SH, Takagi H, Louca D et al (2010) Frustrated magnetism and cooperative phase transitions in spinels. J Phys Soc Jpn 79:1–14. https://doi.org/10.1143/JPSJ.79.011004
36. Mathubala G, Manikandan A, Antony SA, Ramar P (2016) Photocatalytic degradation of methylene blue dye and magneto- optical studies of magnetically recyclable spinel NixMn1-xFe2O4 (x=0.0–1.0) nanoparticles. J Mol Struct 1113:79–87. https://doi.org/10.1016/j.molstruc.2016.02.032
37. Sharma N, Shaju KM, Subba Rao GV, Chowdari BVR (2003) Iron-tin oxides with CaFe2O4 structure as anodes for Li-ion batteries. J Power Sources 124:204–212. https://doi.org/10.1016/S0378-7753(03)00670-0
38. Candeia RA, Bernardi MIB, Longo E et al (2004) Synthesis and characterization of spinel pigment CaFe 2 O 4 obtained by the polymeric precursor method. Mater Lett 58:569–572. https://doi.org/10.1016/S0167-577X(03)00563-9
39. Mekatel E, Trari M, Nibou D et al (2019) Preparation and characterization of A-Fe2O3 supported clay as a novel photocatalyst for hydrogen evolution. Int J Hydrogen Energy 44:10309–10315. https://doi.org/10.1016/j.ijhydene.2019.03.007
40. Abdi A, Trari M (2013) Investigation on photoelectrochemical and pseudo-capacitance properties of the non-stoichiometric hematite α-Fe2O3 elaborated by sol-gel. Electrochim Acta 111:869–875. https://doi.org/10.1016/j.electacta.2013.08.076
41. Ikenaga NO, Ohgaito Y, Suzuki T (2005) H2S absorption behavior of calcium ferrite prepared in the presence of coal. Energy Fuels 19:170–179. https://doi.org/10.1021/ef049907z

42. Miller D, Siriwardane R (2018) CaFe2O4 oxygen carrier characterization during the partial oxidation of coal in the chemical looping gasification application. Appl Energy 224:1–24
43. Li D, Song H, Meng X et al (2020) Effects of particle size on the structure and photocatalytic performance by alkali-treated TiO(2). Nanomaterials (Basel, Switzerland). https://doi.org/10.3390/nano10030546
44. Lahmar H, Benamira M, Douafer S et al (2020) Photocatalytic degradation of methyl orange on the novel hetero-system La2NiO4/ZnO under solar light. Chem Phys Lett 742:137132. https://doi.org/10.1016/j.cplett.2020.137132
45. Jiang Z, Huang S, Qian B (1994) Semiconductor properties of Ag2O film formed on the silver electrode in 1MNaOH solution. Electrochim Acta 39:2465–2470
46. Kenfoud H, Nasrallah N, Baaloudj O et al (2022) Enhanced photocatalytic reduction of Cr(VI) by the novel hetero-system BaFe2O4/SnO2. J Phys Chem Solids 160:110315. https://doi.org/10.1016/j.jpcs.2021.110315
47. Kenfoud H, Nasrallah N, Baaloudj O et al (2020) Photocatalytic reduction of Cr(VI) onto the spinel CaFe2O4 nanoparticles. Optik 223:165610. https://doi.org/10.1016/j.ijleo.2020.165610
48. Sahmi A, Bensadok K, Trari M (2017) Photoelectrochemical properties of CaWO4 synthetized by chemical route: application to the phenobarbital electro-photocatalysis. J Photochem Photobiol, A 349:36–41. https://doi.org/10.1016/j.jphotochem.2017.08.070
49. Hemmi A, Belmedani M, Mekatel E et al (2021) Kinetic and mechanism studies of tetracycline photodegradation using synthesized ZnAl2O4. React Kinet Mech Catal 134:1039–1054. https://doi.org/10.1007/s11144-021-02114-5

Authors and Affiliations

D. Berdous[1] · H. Kenfoud[2] · M. Trari[3]

[1] Hydrometallurgy and Inorganic Molecular Chemistry Laboratory, Chemistry Faculty, (USTHB), BP 32, El-Alia, Algiers, Algeria

[2] Laboratory of Reaction Engineering, Faculty of Mechanical Engineering and Process Engineering, BP 32, 16111 Algiers, USTHB, Algeria

[3] Laboratory of Storage and Valorisation of Renewable Energies, Faculty of Chemistry, (USTHB), BP 32, 16111 Algiers, Algeria